

Portland State University

PDXScholar

University Honors Theses

University Honors College

8-21-2017

Modeling Anisotropy in the Earthquake Cycle: a Numerical Multiscale Model

Maricela T. Best Mckay
Portland State University

Follow this and additional works at: <https://pdxscholar.library.pdx.edu/honorstheses>

Let us know how access to this document benefits you.

Recommended Citation

Best Mckay, Maricela T., "Modeling Anisotropy in the Earthquake Cycle: a Numerical Multiscale Model" (2017). *University Honors Theses*. Paper 467.
<https://doi.org/10.15760/honors.467>

This Thesis is brought to you for free and open access. It has been accepted for inclusion in University Honors Theses by an authorized administrator of PDXScholar. Please contact us if we can make this document more accessible: pdxscholar@pdx.edu.

Modeling Anisotropy in the Earthquake Cycle: A Numerical Multiscale Model

by

Maricela Best McKay

An undergraduate honors thesis submitted in partial
fulfillment of the requirements for the degree of

Bachelor of Science
in
University Honors
and
Mathematics

Thesis Advisor
Dr. Brittany Erickson

Portland State University

2017

Modeling Anisotropy in the Earthquake Cycle: A Numerical Multiscale Model

Maricela Best McKay
Advisor: Dr. Brittany Erickson
Portland State University, 2017

ABSTRACT

We have developed a methodology for incorporating and studying the effects of anisotropy when simulating the full earthquake cycle. The method is developed for a vertical strike-slip fault in two-dimensions, with antiplane motion. Inertial terms are dropped from the elastic anisotropic wave equation to obtain a steady state problem. This resulting equilibrium equation is discretized with a finite difference method. A nonlinear rate-and-state friction law is enforced at the fault. Time stepping is adaptive to capture highly varying time scales, and as such is able to produce self-consistent initial conditions.

Contents

1	Introduction	4
2	Background Mechanics	6
3	Governing Equations	10
4	Semi-Discretization of the Problem	16
4.1	Spatial Accuracy	19
5	Frictional Framework and Time Stepping Method	22
6	Simulations	26
6.1	Parameter Study 1	28
6.2	Parameter Study 2	30
6.3	Conclusion	32
	Bibliography	35

1 | Introduction

Modeling the full earthquake cycle poses unique challenges. Interseismic periods between fault rupture happen on a time scale of hundreds of years, while fault ruptures occur on a time scale of seconds. Additionally, earthquake faults have complex geometries, and the physical makeup of the materials that surround earthquake faults is complex and varying.

Anisotropy is defined as the property of being directionally dependant. In our case, a material is considered anisotropic when its deformation from being subjected to a force, is directionally dependant. This means that it deforms differently when a force is applied in one direction, compared to a force applied in a different direction. To give a concrete example, consider the act of splitting wood into kindling. It is much easier to split a piece of wood when striking it with the grain, than against the grain. This is due to the underlying anisotropic material properties of wood.

The materials of the Earth often exhibit anisotropic properties. Seismic anisotropy has been observed in the Earth's crust, the upper mantle, the transition zone, the D" layer, and the inner core [10]. Seismic anisotropy can be observed through shear wave splitting, that is, when a shear wave splits into two components with different propagation speeds. This splitting has been observed in most igneous, metamorphic, and sedimentary rocks in the Earth's crust [2].

While seismic anisotropy is present in the real world, many models make the simplifying assumption of isotropic material properties. In [1] Erickson and Dunham introduced an efficient numerical method for modeling the full earthquake cycle in isotropic, heterogeneous media. The method was developed for the two-dimensional, antiplane shear problem of a vertical strike-slip fault, in a linear elastic half-space. In this thesis we extend this framework to incorporate anisotropy.

In Chapter 2 we briefly introduce linear elasticity theory, and derive the anisotropic elastic 2D equation for motion. In Chapter 3 we introduce the governing equations

that are solved by our numerical model, and prove the well-posedness of the continuous problem via the energy method. In Chapter 4 we discretize the problem, and show spatial convergence of the numerical discretization, by manufacturing a solution and testing correct order of convergence. In Chapter 5 we discuss the time stepping method of the problem, and the boundary conditions. In Chapter 6 we discuss the parameters chosen for the preliminary study presented in this thesis, show some initial results, and conclude the thesis.

2 | Background Mechanics

The model of the earthquake cycle presented in this thesis is built on linear elasticity theory. Linear elasticity theory is a subest of continuum mechanics, wherein objects are modeled as continuous rather than discrete. Consider a force applied to an object at every point of its continuum. External forces act on the object to deform it, while internal forces resist this deformation. The object is said to have elastic material properties if it completely recovers to its original pre-deformed shape when the external forces are removed. In modeling an object with linear elasticity, we assume that on an infinitesimally small scale, stress may be treated as linearly related to the strain. The constitutive law that describes this relationship is Hooke's law.

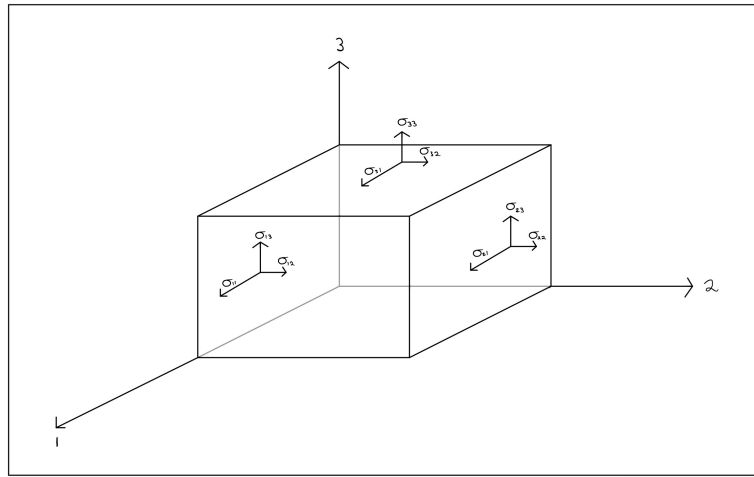


Figure 2.0.1: Components of the stresses acting on the three faces of a cube

Hooke's law can be written as $\sigma_{ij} = C_{ijkl}\epsilon_{kl}$, where i, j, k, l assume the values x, y, z . σ_{ij} denotes the stress tensor, C_{ijkl} the material stiffness tensor, and ϵ_{ij} the strain tensor. The stress tensor has components σ_{ij} that act on the i th plane in the j th direction. This means that stress components with repeated indices act as normal

stresses, while the other components of the stress tensor act as shear stresses. Additionally, stress tensor components satisfy that $\sigma_{ij} = \sigma_{ji}$. Components of the stress tensor acting on an cube are illustrated in Figure 2.0.1. The strain tensor can be thought of as a tensor that contains information about the deformation of an object. Hooke's law tells us that these strains are linearly related to the stresses. This means that the strain tensor has the same properties as the stress tensor, in that components with repeated indices ϵ_{kk} are normal strains, components with differing indices ϵ_{ij} are shear strains, and $\epsilon_{ij} = \epsilon_{ji}$.

The fourth order stiffness tensor C_{ijkl} has 81 entries in its most general form, however the symmetric properties of stress and strain reduce the number of independent entries of the stiffness tensor down to 36, with the symmetries $C_{ijkl} = C_{jikl} = C_{jilk}$. Additionally, the number of independent entries reduces further to 21, due to the requirement that $C_{ijkl} = C_{klij}$. The symmetric properties of the stress and strain tensors mean that we may write Hooke's law as

$$\begin{bmatrix} \sigma_{xx} \\ \sigma_{yy} \\ \sigma_{zz} \\ \sigma_{yz} \\ \sigma_{xy} \\ \sigma_{xz} \end{bmatrix} = \begin{bmatrix} C_{xxxx} & C_{xxyy} & C_{xxzz} & C_{xxyz} & C_{xxzx} & C_{xxxy} \\ C_{yyxx} & C_{yyyy} & C_{yyzz} & C_{yyyz} & C_{yyzx} & C_{yyxy} \\ C_{zzxx} & C_{zzyy} & C_{zzzz} & C_{zzyz} & C_{zzzx} & C_{zzxy} \\ C_{yzxx} & C_{yzyy} & C_{yzzz} & C_{yzyz} & C_{yzzx} & C_{yzxy} \\ C_{xyxx} & C_{xyyy} & C_{xyzz} & C_{xyyz} & C_{xyzx} & C_{xyxy} \\ C_{xzxz} & C_{xzyy} & C_{xzzz} & C_{xzyz} & C_{xzzx} & C_{xzxy} \end{bmatrix} \begin{bmatrix} \epsilon_{xx} \\ \epsilon_{yy} \\ \epsilon_{zz} \\ 2\epsilon_{yz} \\ 2\epsilon_{xy} \\ 2\epsilon_{xz} \end{bmatrix} \quad (2.0.1)$$

Consider the displacement of a body in space given by $u(x, y, z)$. The strain on the displaced body is then expressed in terms of displacement as

$$\epsilon_{ij} = \frac{1}{2} \left(\frac{\partial u_i}{\partial j} + \frac{\partial u_j}{\partial i} \right).$$

Then Eq. 2.0.1 becomes

$$\begin{bmatrix} \sigma_{xx} \\ \sigma_{yy} \\ \sigma_{zz} \\ \sigma_{yz} \\ \sigma_{xy} \\ \sigma_{xz} \end{bmatrix} = \begin{bmatrix} C_{xxxx} \frac{\partial u_x}{\partial x} + C_{xxyy} \left(\frac{\partial u_x}{\partial y} + \frac{\partial u_y}{\partial x} \right) + C_{xxyy} \frac{\partial u_y}{\partial y} + C_{xxyz} \left(\frac{\partial u_y}{\partial z} + \frac{\partial u_z}{\partial y} \right) + C_{xxzx} \left(\frac{\partial u_x}{\partial z} + \frac{\partial u_z}{\partial x} \right) + C_{xxzz} \frac{\partial u_z}{\partial z} \\ C_{yyxx} \frac{\partial u_x}{\partial x} + C_{yyyy} \left(\frac{\partial u_x}{\partial y} + \frac{\partial u_y}{\partial x} \right) + C_{yyyy} \frac{\partial u_y}{\partial y} + C_{yyyz} \left(\frac{\partial u_y}{\partial z} + \frac{\partial u_z}{\partial y} \right) + C_{yyzx} \left(\frac{\partial u_x}{\partial z} + \frac{\partial u_z}{\partial x} \right) + C_{yyzz} \frac{\partial u_z}{\partial z} \\ C_{zzxx} \frac{\partial u_x}{\partial x} + C_{zzxy} \left(\frac{\partial u_x}{\partial y} + \frac{\partial u_y}{\partial x} \right) + C_{zzyy} \frac{\partial u_y}{\partial y} + C_{zzyz} \left(\frac{\partial u_y}{\partial z} + \frac{\partial u_z}{\partial y} \right) + C_{zzzx} \left(\frac{\partial u_x}{\partial z} + \frac{\partial u_z}{\partial x} \right) + C_{zzzz} \frac{\partial u_z}{\partial z} \\ C_{yzxx} \frac{\partial u_x}{\partial x} + C_{yzyy} \left(\frac{\partial u_x}{\partial y} + \frac{\partial u_y}{\partial x} \right) + C_{yzyy} \frac{\partial u_y}{\partial y} + C_{yzyz} \left(\frac{\partial u_y}{\partial z} + \frac{\partial u_z}{\partial y} \right) + C_{yzzx} \left(\frac{\partial u_x}{\partial z} + \frac{\partial u_z}{\partial x} \right) + C_{yzzz} \frac{\partial u_z}{\partial z} \\ C_{xyxx} \frac{\partial u_x}{\partial x} + C_{xyyy} \left(\frac{\partial u_x}{\partial y} + \frac{\partial u_y}{\partial x} \right) + C_{xyyy} \frac{\partial u_y}{\partial y} + C_{xyyz} \left(\frac{\partial u_y}{\partial z} + \frac{\partial u_z}{\partial y} \right) + C_{xyzx} \left(\frac{\partial u_x}{\partial z} + \frac{\partial u_z}{\partial x} \right) + C_{xyzz} \frac{\partial u_z}{\partial z} \\ C_{xzxz} \frac{\partial u_x}{\partial x} + C_{xzyy} \left(\frac{\partial u_x}{\partial y} + \frac{\partial u_y}{\partial x} \right) + C_{xzyy} \frac{\partial u_y}{\partial y} + C_{xzyz} \left(\frac{\partial u_y}{\partial z} + \frac{\partial u_z}{\partial y} \right) + C_{xzzx} \left(\frac{\partial u_x}{\partial z} + \frac{\partial u_z}{\partial x} \right) + C_{xzzz} \frac{\partial u_z}{\partial z} \end{bmatrix}. \quad (2.0.2)$$

Newton's second law of motion, Force=Mass·Acceleration, can be written as

$$\nabla \cdot \sigma + \rho b = \rho \frac{\partial^2 u}{\partial t^2}$$

where u is the vector of displacements, i.e. $u = [u_x, u_y, u_z]^T$. In the absence of body forces this simplifies to

$$\nabla \cdot \sigma = \rho \frac{\partial^2 u}{\partial t^2}. \quad (2.0.3)$$

Written out in full we have

$$\rho \frac{\partial^2 u_x}{\partial t^2} = \frac{\partial \sigma_{xx}}{\partial x} + \frac{\partial \sigma_{xy}}{\partial y} + \frac{\partial \sigma_{xz}}{\partial z} \quad (2.0.4a)$$

$$\rho \frac{\partial^2 u_y}{\partial t^2} = \frac{\partial \sigma_{xy}}{\partial x} + \frac{\partial \sigma_{yy}}{\partial y} + \frac{\partial \sigma_{yz}}{\partial z} \quad (2.0.4b)$$

$$\rho \frac{\partial^2 u_z}{\partial t^2} = \frac{\partial \sigma_{xz}}{\partial x} + \frac{\partial \sigma_{yz}}{\partial y} + \frac{\partial \sigma_{zz}}{\partial z}. \quad (2.0.4c)$$

Now consider the 2-D case, where the only non-zero component of displacement is in the out-of-plane direction u_z , and is only dependent on the other two directions; in other words $u_y = u_x = 0$ and $u_z = u_z(y, z)$. Then Eq. 2.0.3 reduces to Eq. 2.0.4a, and Eq. 2.0.2 simplifies to

$$\begin{aligned} \sigma_{xx} &= c_{xxxy} \frac{\partial u_z}{\partial y} + c_{xxzx} \frac{\partial u_z}{\partial z} \\ \sigma_{xy} &= c_{xyxy} \frac{\partial u_z}{\partial y} + c_{xyzx} \frac{\partial u_z}{\partial z} \\ \sigma_{xz} &= c_{xzyy} \frac{\partial u_z}{\partial y} + c_{xzxx} \frac{\partial u_z}{\partial z}. \end{aligned}$$

Substituting this into Eq. 2.0.4a we get

$$\rho \frac{\partial^2 u_z}{\partial t^2} = \frac{\partial}{\partial x} \left(c_{xxxy} \frac{\partial u_z}{\partial y} + c_{xxzx} \frac{\partial u_z}{\partial z} \right) + \frac{\partial}{\partial y} \left(c_{xyxy} \frac{\partial u_z}{\partial y} + c_{xyzx} \frac{\partial u_z}{\partial z} \right) + \frac{\partial}{\partial z} \left(c_{xzyy} \frac{\partial u_z}{\partial y} + c_{xzxx} \frac{\partial u_z}{\partial z} \right).$$

Because $u_x = u_x(y, z)$, this further simplifies to

$$\rho \frac{\partial^2 u_x}{\partial t^2} = \frac{\partial}{\partial y} \left(c_{xyxy} \frac{\partial u_x}{\partial y} + c_{xyzx} \frac{\partial u_x}{\partial z} \right) + \frac{\partial}{\partial z} \left(c_{xzyx} \frac{\partial u_x}{\partial y} + c_{xzzx} \frac{\partial u_x}{\partial z} \right). \quad (2.0.5)$$

Note that the symmetry properties of stiffness tensor C mean that $c_{xyxz} = c_{xzyx}$. We have now derived the 2D anisotropic wave equation.

3 | Governing Equations

We will now denote u_x as simply u . We assume that coefficients $c_{xyxy}, c_{xyzx}, c_{xzzx}$ are constants which means that we can write Eq. 2.0.5 as

$$\rho \frac{\partial^2 u}{\partial t^2} = \mu_1 \frac{\partial^2 u}{\partial y^2} + 2\mu_2 \frac{\partial^2 u}{\partial y \partial z} + \mu_3 \frac{\partial^2 u}{\partial z^2} \quad (y, z) \in [-L_y, L_y] \times [0, L_z]. \quad (3.0.1)$$

This corresponds to antiplane shear deformation, where the only non-zero component of displacement is in the out-of-plane direction x . The symmetric properties of the field $u(y, z, t)$ about the interface $y = 0$ mean that we may restrict our problem to the right-hand side of the domain $\Omega = [0, L_y] \times [0, L_z]$. We apply traction-free boundary conditions at the top and bottom boundaries of the domain, and Dirichlet boundary conditions at the left and right boundaries. The traction vector at a given boundary is found by taking the dot product of the vector normal to the boundary and the stress tensor. A traction-free boundary condition then corresponds to setting the all components of the traction vector at the top and bottom boundaries to zero.

We can write the left, right, top, and bottom boundary data in the respective general forms g_f, g_r, g_s , and g_d . We then have the following formulation:

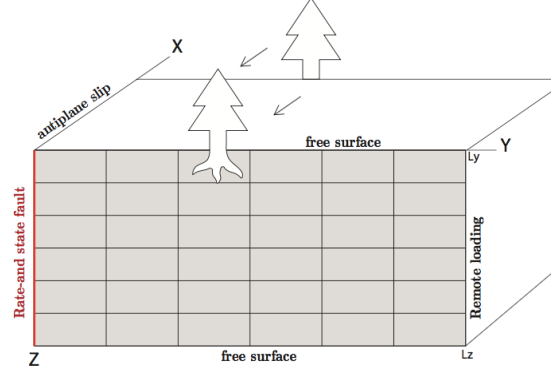
$$u(0, z, t) = g_l(z, t) \quad (3.0.2)$$

$$u(L_y, z, t) = g_r(z, t) \quad (3.0.3)$$

$$\mu_2 \frac{\partial u}{\partial y} \Big|_{z=0} + \mu_3 \frac{\partial u}{\partial z} \Big|_{z=0} = g_t(y, t) \quad (3.0.4)$$

$$\mu_2 \frac{\partial u}{\partial y} \Big|_{z=L_z} + \mu_3 \frac{\partial u}{\partial z} \Big|_{z=L_z} = g_b(y, t) \quad (3.0.5)$$

The figure below illustrates the problem setup, showing a 3D schematic of the 2D model which illustrates the out-of-plane motion.



The goal is to model a physical phenomena; as such it is important to establish that the problem well-posed. This means that the problem satisfies the following conditions:

1. The solution exists
2. The solution is unique
3. The solution depends continuously on the data.

To establish the well-posedness of the continuous problem we employ the energy method, setting the boundary data to zero in order to simplify the analysis. These results can be extended to non-zero boundary data by invoking Duhamel's principle.

The energy method is applied to 3.0.1; we multiply by $\frac{\partial u}{\partial t}$ and integrate

$$\begin{aligned} \iint_{00}^{L_z L_y} \rho \frac{\partial u}{\partial t} \frac{\partial^2 u}{\partial t^2} dy dz &= \iint_{00}^{L_z L_y} \mu_1 \frac{\partial u}{\partial t} \frac{\partial^2 u}{\partial y^2} dy dz + \iint_{00}^{L_z L_y} \mu_2 \frac{\partial u}{\partial t} \frac{\partial^2 u}{\partial y \partial z} dy dz + \dots \\ &\quad \iint_{00}^{L_z L_y} \mu_2 \frac{\partial u}{\partial t} \frac{\partial^2 u}{\partial y \partial z} dy dz + \iint_{00}^{L_z L_y} \mu_3 \frac{\partial u}{\partial t} \frac{\partial^2 u}{\partial z^2} dy dz \end{aligned} \quad (3.0.6)$$

Which simplifies to

$$\begin{aligned}
\frac{1}{2} \frac{\partial}{\partial t} \left\| \sqrt{\rho} \frac{\partial u}{\partial t} \right\|^2 &= \int_0^{L_z} \mu_1 \frac{\partial u}{\partial t} \frac{\partial u}{\partial y} \Big|_0^{L_y} dz - \iint_{00}^{L_y L_z} \mu_1 \frac{\partial^2 u}{\partial t \partial y} \frac{\partial u}{\partial y} dz dy + \int_0^{L_z} \mu_2 \frac{\partial u}{\partial t} \frac{\partial u}{\partial y} \Big|_0^{L_y} dz - \dots \\
&\quad \iint_{00}^{L_y L_z} \mu_2 \frac{\partial^2 u}{\partial t \partial z} \frac{\partial u}{\partial y} dz dy + \int_0^{L_y} \mu_2 \frac{\partial u}{\partial t} \frac{\partial u}{\partial z} \Big|_0^{L_z} dy - \iint_{00}^{L_z L_y} \mu_2 \frac{\partial^2 u}{\partial t \partial y} \frac{\partial u}{\partial z} dy dz + \dots \\
&\quad \int_0^{L_y} \mu_3 \frac{\partial u}{\partial t} \frac{\partial u}{\partial z} \Big|_0^{L_z} dy - \iint_{00}^{L_z L_y} \mu_3 \frac{\partial^2 u}{\partial t \partial z} \frac{\partial u}{\partial z} dy dz. \tag{3.0.7}
\end{aligned}$$

Let,

$$\begin{aligned}
B_r &= \int_0^{L_z} \mu_1 \frac{\partial u}{\partial t} \frac{\partial u}{\partial y} \Big|_{L_y} dz + \int_0^{L_z} \mu_2 \frac{\partial u}{\partial t} \frac{\partial u}{\partial y} \Big|_{L_y} dz \\
B_f &= - \left(\int_0^{L_z} \mu_1 \frac{\partial u}{\partial t} \frac{\partial u}{\partial y} \Big|_0 dz + \int_0^{L_z} \mu_2 \frac{\partial u}{\partial t} \frac{\partial u}{\partial y} \Big|_0 dz \right) \\
B_d &= \int_0^{L_y} \mu_2 \frac{\partial u}{\partial t} \frac{\partial u}{\partial z} \Big|_{L_z} dy + \int_0^{L_y} \mu_3 \frac{\partial u}{\partial t} \frac{\partial u}{\partial z} \Big|_{L_z} dy \\
B_s &= - \left(\int_0^{L_y} \mu_2 \frac{\partial u}{\partial t} \frac{\partial u}{\partial z} \Big|_0 dy + \int_0^{L_y} \mu_3 \frac{\partial u}{\partial t} \frac{\partial u}{\partial z} \Big|_0 dy \right).
\end{aligned}$$

Then 3.0.6 reduces to

$$\begin{aligned}
\frac{1}{2} \frac{\partial}{\partial t} \left\| \rho \frac{\partial u}{\partial t} \right\|^2 &= B_r + B_l + B_t + B_b - \dots \\
&\quad \left(\iint_{00}^{L_z L_y} \frac{\partial u}{\partial y} \left[\frac{\partial}{\partial t} \left(\mu_1 \frac{\partial u}{\partial z} + \mu_2 \frac{\partial u}{\partial y} \right) \right] dy dz + \iint_{00}^{L_z L_y} \frac{\partial u}{\partial z} \left[\frac{\partial}{\partial t} \left(\mu_2 \frac{\partial u}{\partial z} + \mu_3 \frac{\partial u}{\partial y} \right) \right] dy dz \right).
\end{aligned}$$

Note that

$$\begin{bmatrix} \frac{\partial u}{\partial y} & \frac{\partial u}{\partial z} \end{bmatrix} \begin{bmatrix} \mu_1 & \mu_2 \\ \mu_2 & \mu_3 \end{bmatrix} \begin{bmatrix} \frac{\partial u}{\partial y} \\ \frac{\partial u}{\partial z} \end{bmatrix} = \mu_1 \frac{\partial u^2}{\partial y} + \mu_2 \frac{\partial u}{\partial z} \frac{\partial u}{\partial y} + \mu_2 \frac{\partial u}{\partial y} \frac{\partial u}{\partial z} + \mu_3 \frac{\partial u^2}{\partial z}.$$

As well as

$$\frac{\partial}{\partial t} \left(\mu_1 \frac{\partial u^2}{\partial y} + \mu_2 \frac{\partial u}{\partial z} \frac{\partial u}{\partial y} + \mu_2 \frac{\partial u}{\partial y} \frac{\partial u}{\partial z} + \mu_3 \frac{\partial u^2}{\partial z} \right) = 2 \frac{\partial u}{\partial y} \left[\frac{\partial}{\partial t} \left(\mu_1 \frac{\partial u}{\partial z} + \mu_2 \frac{\partial u}{\partial y} \right) \right] + 2 \frac{\partial u}{\partial z} \left[\frac{\partial}{\partial t} \left(\mu_2 \frac{\partial u}{\partial z} + \mu_3 \frac{\partial u}{\partial y} \right) \right].$$

Now we have that

$$\frac{1}{2} \frac{\partial}{\partial t} \|\rho u_t\|^2 = B_r + B_s + B_d + B_f - \frac{1}{2} \frac{\partial}{\partial t} \iint_{00}^{L_y L_z} \begin{bmatrix} \frac{\partial u}{\partial y} & \frac{\partial u}{\partial z} \end{bmatrix} \begin{bmatrix} \mu_1 & \mu_2 \\ \mu_2 & \mu_3 \end{bmatrix} \begin{bmatrix} \frac{\partial u}{\partial y} \\ \frac{\partial u}{\partial z} \end{bmatrix} dz dy. \quad (3.0.8)$$

Define $\|\mathbf{U}\|_\mu = \sqrt{\mathbf{U}^T \mathbf{M} \mathbf{U}}$, where $\mathbf{U} = \begin{bmatrix} \frac{\partial u}{\partial y} \\ \frac{\partial u}{\partial z} \end{bmatrix}$ and $\mathbf{M} = \begin{bmatrix} \mu_1 & \mu_2 \\ \mu_2 & \mu_3 \end{bmatrix}$. Then $\|\mathbf{U}\|_\mu$ defines a norm.

Indeed, $\mathbf{U}^T \mathbf{M} \mathbf{U}$ is a quadratic form, which means that it satisfies

$$\lambda_{\min} \|\mathbf{U}\|^2 \leq \mathbf{U}^T \mathbf{M} \mathbf{U} \leq \lambda_{\max} \|\mathbf{U}\|^2$$

where $\|\mathbf{U}\|$ refers to the L_2 norm of \mathbf{U} , λ_{\min} is the smallest eigenvalue of \mathbf{M} , and λ_{\max} is the largest eigenvalue of \mathbf{M} . \mathbf{M} is a positive definite matrix, which means that both λ_{\max} and λ_{\min} are non-negative. Therefore, $\mathbf{U}^T \mathbf{M} \mathbf{U}$ is positive and $\mathbf{U}^T \mathbf{M} \mathbf{U} = 0$ if and only if $\mathbf{U} = 0$.

Let $\alpha \in \mathbb{R}$

$$\begin{aligned}
\|\alpha \mathbf{U}\|_\mu &= \sqrt{\begin{bmatrix} \alpha \frac{\partial u}{\partial y} & \alpha \frac{\partial u}{\partial z} \end{bmatrix} \begin{bmatrix} \mu_1 & \mu_2 \\ \mu_2 & \mu_3 \end{bmatrix} \begin{bmatrix} \alpha \frac{\partial u}{\partial y} \\ \alpha \frac{\partial u}{\partial z} \end{bmatrix}} \\
&= \sqrt{\alpha^2 \mu_1 \frac{\partial u^2}{\partial y} + 2\alpha^2 \mu_2 \frac{\partial u}{\partial y} \frac{\partial u}{\partial z} + \alpha^2 \mu_3 \frac{\partial u^2}{\partial z}} \\
&= |\alpha| \sqrt{\mu_1 \frac{\partial u^2}{\partial y} + 2\mu_2 \frac{\partial u}{\partial y} \frac{\partial u}{\partial z} + \mu_3 \frac{\partial u^2}{\partial z}} \\
&= |\alpha| \|\mathbf{U}\|_\mu
\end{aligned}$$

Let $\mathbf{V} = \begin{bmatrix} \frac{\partial v}{\partial y} \\ \frac{\partial v}{\partial z} \end{bmatrix}$ and consider $\|\mathbf{U} + \mathbf{V}\|_\mu^2$. Then

$$\begin{aligned}
\|\mathbf{U} + \mathbf{V}\|_\mu^2 &= (\mathbf{U} + \mathbf{V})^T \mathbf{M} (\mathbf{U} + \mathbf{V}) \\
&= (\mathbf{U} + \mathbf{V})^T (\mathbf{M}\mathbf{U} + \mathbf{M}\mathbf{V}) \\
&= \mathbf{U}^T \mathbf{M}\mathbf{U} + \mathbf{U}^T \mathbf{M}\mathbf{V} + \mathbf{V}^T \mathbf{M}\mathbf{U} + \mathbf{V}^T \mathbf{M}\mathbf{V} \\
&= \|\mathbf{U}\|_\mu^2 + 2\mathbf{V}^T \mathbf{M}\mathbf{U} + \|\mathbf{V}\|_\mu^2 \\
&= \|\mathbf{U}\|_\mu^2 + 2\sqrt{\mathbf{V}^T \mathbf{M}\mathbf{U} \mathbf{V}^T \mathbf{M}\mathbf{U}} + \|\mathbf{V}\|_\mu^2 \\
&= \|\mathbf{U}\|_\mu^2 + 2\sqrt{\mathbf{V}^T \mathbf{M}\mathbf{V} \mathbf{U}^T \mathbf{M}\mathbf{U}} + \|\mathbf{V}\|_\mu^2 \\
&= \|\mathbf{U}\|_\mu^2 + 2\sqrt{\|\mathbf{V}\|_\mu^2 \|\mathbf{U}\|_\mu^2} + \|\mathbf{V}\|_\mu^2 \\
&= \|\mathbf{U}\|_\mu^2 + 2\|\mathbf{V}\|_\mu \|\mathbf{U}\|_\mu + \|\mathbf{V}\|_\mu^2 \\
&= (\|\mathbf{U}\|_\mu + \|\mathbf{V}\|_\mu)^2
\end{aligned}$$

Thus, we have shown $\|\mathbf{U}\|_\mu$ is a norm.

Now consider,

$$\|\mathbf{U}\|_M = \iint_{00}^{L_z L_y} \sqrt{\mathbf{U}^T \mathbf{M}\mathbf{U}} \, dy \, dz \quad (3.0.9)$$

Because $\Omega = [0, L_y] \times [0, L_z]$ is non-negative, it follows, by the linearity of integration, that $\|\mathbf{U}\|_M$ is a norm on Ω .

We have now completed the energy method, since we can write 3.0.8 as

$$\frac{1}{2} \frac{\partial}{\partial t} \left(\left\| \sqrt{\rho} \frac{\partial u}{\partial t} \right\|^2 + \left\| \begin{bmatrix} \frac{\partial u}{\partial y} & \frac{\partial u}{\partial z} \end{bmatrix} \right\|_M^2 \right) = B_r + B_s + B_d + B_f \quad (3.0.10)$$

For zero boundary data, B_r, B_s, B_d , and B_f vanish. We have established that the continuous problem is well-posed. The left-hand side of 3.0.10 is the norm on the rate of change of the total energy (the sum of the kinetic and strain energy), while B_r, B_s, B_d , and B_f represents the rate of work done on the elastic body by the traction at each of the boundaries. The energy method then represents the conservation of energy of the system.

4 | Semi-Discretization of the Problem

We now turn our attention to solving the problem that we set up in the previous section. To simulate the earthquake cycle we must solve Eqs. (3.0.1-3.0.5) numerically. This requires that we discretize our problem. We begin by discretizing in space only. We leave the discretization of time alone for now, coming back to it in the next chapter. Our goal is to find a semi-discretization, meaning a discretization in space that leaves time continuous, of Eqs. (3.0.1-3.0.5).

The domain of the problem $\Omega = [0, L_y] \times [0, L_z]$ is discretized into an evenly spaced grid. In the y direction we denote the grid spacing h_y and in the z direction we denote it h_z . A discrete grid point (y_i, z_i) is defined to be (ih_y, jh_z) , where $i \in [0, N_y] \subset \mathbb{N}$ and $j \in [0, N_z] \subset \mathbb{N}$. This means we can write the grid spacing in each direction as $h_y = \frac{L_y}{N_y}$ and $h_z = \frac{L_z}{N_z}$. The numerical approximation to the solution u can then be expressed as $u_{ij} \approx u(t, y_i, z_j)$.

Let \mathbf{u} be a grid vector of the approximate solution at each gridpoint, where the gridpoints are stacked vertically as follows. Define $\mathbf{u}_l = [u_{l,0}, u_{l,1}, \dots, u_{l,N_z}]^T$, where $l \in [0, N_y] \subset \mathbb{N}$, then $\mathbf{u} = [\mathbf{u}_0^T, \mathbf{u}_1^T, \dots, \mathbf{u}_{N_y}^T]^T$.

The derivatives in Eq. 3.0.1 are numerically approximated with summation-by-parts (SBP) finite difference operators. These are matrix operators that are designed to mimic integration-by-parts discretely. The desirable summation-by-parts properties of these operators require that special consideration be given to enforcement of the boundary conditions. Setting the boundary conditions explicitly by injecting the boundary data into the grid vector fails to preserve the desired SBP properties. Instead, the boundary terms are weakly enforced via the use of penalty terms. These penalty terms are similar to those employed in discontinuous Galerkin Finite Element methods, such as Nitsche's method. In the SBP framework, a penalty term can be

thought of as acting like a spring that keeps the approximated numerical boundary sufficiently close, though not necessarily equal to, the desired boundary data. The grid vector at the boundary is penalized for straying too far from the actual boundary condition. [6]

The Kronecker product is very useful in the discretization of Eqs. (3.0.1-3.0.5), so we briefly define it:

Let \mathbf{A} be an $m \times n$ matrix and \mathbf{B} be an $l \times k$ matrix. The Kronecker product of matrices \mathbf{A} and \mathbf{B} is defined

$$\mathbf{A} \otimes \mathbf{B} = \begin{bmatrix} a_{0,0}\mathbf{B} & \dots & a_{0,m}\mathbf{B} \\ \vdots & \ddots & \vdots \\ a_{m,0}\mathbf{B} & \dots & a_{m,n}\mathbf{B} \end{bmatrix}$$

where $\mathbf{A} \otimes \mathbf{B}$ is an $ml \times nk$ matrix.

Let \mathbf{I} denote the identity matrix, and let a z or y subscript denote the direction a matrix operator is acting in. Then \mathbf{I}_z , for example, is the identity operator acting in the z direction. With this in mind, the discretization of Eqs. (3.0.1-3.0.5) is:

$$\rho u_{tt} = \mu_1 \mathbf{D}_{2z} \mathbf{u} + 2\mu_2 \mathbf{D}_{yz} \mathbf{u} + \mu_3 \mathbf{D}_{2z} \mathbf{u} + \mathbf{p}_f + \mathbf{p}_r + \mathbf{p}_s + \mathbf{p}_d \quad (4.0.1)$$

where,

$$\mathbf{D}_{yz} = \mathbf{D}_y \otimes \mathbf{D}_z \quad (4.0.2)$$

$$\mathbf{D}_{2y} = \mathbf{D}_2 \otimes \mathbf{I}_z$$

$$\mathbf{D}_{2z} = \mathbf{I}_y \otimes \mathbf{D}_2$$

\mathbf{D}_2 is a second order accurate, SBP operator that approximates the second derivative. In its interior, operator \mathbf{D}_2 , uses the standard centered difference approximation to the second derivative. \mathbf{D}_2 is given by

$$\mathbf{D}_2 = \mathbf{H}^{-1}(-\mathbf{M} + \mathbf{B}\mathbf{S}) \quad (4.0.3)$$

where $\mathbf{M} = \mathbf{D}_1^T \mathbf{H} \mathbf{D}_1$.

Because SBP operators are designed to mimic integration by parts discretely, weight

matrix $\mathbf{H} = h \begin{bmatrix} \frac{1}{2} & 0 & \dots & \dots & 0 \\ 0 & 1 & 0 & \dots & \vdots \\ \vdots & 0 & \ddots & 0 & \vdots \\ \vdots & \vdots & 0 & 1 & 0 \\ 0 & \dots & \dots & 0 & \frac{1}{2} \end{bmatrix}$ defines a quadrature rule. For any given functions $u, w \in \mathbb{R}^n$ and $a, b \in \mathbb{R}$, $\int_a^b uw \, dx \approx \mathbf{u}^T \mathbf{H} \mathbf{w}$ [8].

\mathbf{D}_1 is an SBP operator that approximates the first derivative with $\mathbf{D}_1 = \mathbf{H}^{-1} \mathbf{Q} \approx \frac{\partial u}{\partial x}$ where $\mathbf{Q} = \begin{bmatrix} -\frac{1}{2} & \frac{1}{2} & 0 & \dots & 0 \\ -\frac{1}{2} & 0 & \frac{1}{2} & 0 & \vdots \\ 0 & \vdots & \ddots & \vdots & 0 \\ \vdots & \vdots & -\frac{1}{2} & 0 & \frac{1}{2} \\ 0 & \dots & 0 & -\frac{1}{2} & \frac{1}{2} \end{bmatrix}$.

Matrix \mathbf{B} zeroes out all but the first and last row of any matrix it is multiplied with, while \mathbf{S} is a matrix operator that approximates the first derivative at the boundaries.

$$\text{Matrix } \mathbf{B} = \begin{bmatrix} -1 & 0 & \dots & 0 \\ 0 & \vdots & \vdots & \vdots \\ \vdots & \vdots & \vdots & 0 \\ 0 & \dots & 0 & 1 \end{bmatrix} \text{ and matrix } \mathbf{S} = \frac{1}{h} \begin{bmatrix} -\frac{3}{2} & 2 & -\frac{1}{2} & & \\ & 1 & & & \\ & & \ddots & & \\ & & & 1 & \\ & & & \frac{1}{2} - 2 & \frac{3}{2} \end{bmatrix}.$$

As described above, SBP methods require that boundary conditions be enforced weakly. This weak enforcement is obtained through the use of penalty vectors called simultaneous approximation terms (SATs) [6]. For our problem boundary conditions (3.0.3-3.0.5) are discretized with SAT penalty vectors \mathbf{p}_f , \mathbf{p}_r , \mathbf{p}_s , and \mathbf{p}_d . Where

$$\mathbf{p}_f = (\mathbf{H}_y^{-1} \otimes \mathbf{I}_z) (\Phi_f + \beta (\mathbf{I}_y \otimes \mathbf{H}_z^{-1}) (\mathbf{I}_z \otimes \mathbf{B}_y \mathbf{S}_y)^T (\mathbf{I}_y \otimes \mathbf{H}_z)) (\mathbf{E}_f \otimes \mathbf{I}_z) (\mathbf{u}_f - \mathbf{g}_f) \quad (4.0.4)$$

$$\mathbf{p}_r = \mathbf{p}_f = (\mathbf{H}_y^{-1} \otimes \mathbf{I}_z) (\Phi_f + \beta (\mathbf{I}_y \otimes \mathbf{H}_z^{-1}) (\mathbf{I}_z \otimes \mathbf{B}_y \mathbf{S}_y)^T (\mathbf{I}_y \otimes \mathbf{H}_z)) (\mathbf{E}_r \otimes \mathbf{I}_z) (\mathbf{u}_r - \mathbf{g}_r) \quad (4.0.5)$$

$$\mathbf{p}_s = \alpha_s (\mathbf{I}_y \otimes \mathbf{H}_z^{-1}) \mathbf{E}_s ([(\mathbf{I}_y \otimes \mathbf{B}_z \mathbf{S}_z) \mathbf{u}]_s + \mathbf{g}_s) \quad (4.0.6)$$

$$\mathbf{p}_d = \alpha_d (\mathbf{I}_y \otimes \mathbf{H}_z^{-1}) \mathbf{E}_d ([(\mathbf{I}_y \otimes \mathbf{B}_z \mathbf{S}_z) \mathbf{u}]_d - \mathbf{g}_d). \quad (4.0.7)$$

Operators $\mathbf{E}_f, \mathbf{E}_r, \mathbf{E}_s$, and \mathbf{E}_d are given by

$$\begin{aligned}\mathbf{E}_f &= \mathbf{e}_0^y \otimes \mathbf{I}_z, & \mathbf{E}_r &= \mathbf{e}_N^y \otimes \mathbf{I}_z \\ \mathbf{E}_s &= \mathbf{I}_y \otimes \mathbf{e}_0^z, & \mathbf{E}_d &= \mathbf{I}_y \otimes \mathbf{e}_N^z\end{aligned}$$

where $\mathbf{e}_0^z = [1, 0, 0, \dots, 0]^T, \mathbf{e}_N^z = [0, 0, 0, \dots, 1]^T$, $\mathbf{e}_0^y = [1, 0, 0, \dots, 0]^T$ and $\mathbf{e}_N^y = [0, 0, 0, \dots, 1]^T$. Constants α_s, α_d , and β are penalty terms. Φ is a matrix that also acts as a penalty term. It is defined in the following way: $\Phi = \phi \mathbf{I}_z \otimes \phi \mathbf{I}_z$, where $\phi = -\frac{30}{11} \frac{\mu_1^2}{\lambda h_y} - \frac{2\mu_3^2}{\lambda h_y}$ and $\lambda = \frac{1}{2}(\mu_1 + \mu_3) - \sqrt{(\mu_1 - \mu_3)^2 + 4\mu_2^2}$.

Penalty terms $\alpha_s, \alpha_d, \beta$, and Φ are adapted from [19] to suit our particular use case of constant anisotropic coefficients. Virta and Mattson prove that their discretization in [19] is stable. Their results hold for our problem, so we omit the proof that the discretization given here is stable.

4.1 Spatial Accuracy

In order to test the spatial accuracy of the discretization, we employ the method of manufactured solutions [15]. We construct a solution u^* to the following problem:

$$\mu_1 \frac{\partial^2 u^*}{\partial y^2} + 2\mu_2 \frac{\partial^2 u^*}{\partial y \partial z} + \mu_3 \frac{\partial^2 u^*}{\partial z^2} = f(y, z) \quad (y, z) \in [0, L_y] \times [0, L_z] \quad (4.1.1a)$$

$$u^*(0, z) = g_f(z) \quad (4.1.1b)$$

$$u^*(L_y, z) = g_r(z) \quad (4.1.1c)$$

$$\left(\mu_2 \frac{\partial u^*}{\partial y} + \mu_3 \frac{\partial u^*}{\partial z} \right) \Big|_{z=0} = 0 \quad (4.1.1d)$$

$$\left(\mu_2 \frac{\partial u^*}{\partial y} + \mu_3 \frac{\partial u^*}{\partial z} \right) \Big|_{z=L_z} = 0 \quad (4.1.1e)$$

where boundary conditions Eqs. (4.1.1c-4.1.1e) match those of the original problem, Dirichlet boundary conditions are enforced at the fault and remote boundaries, and traction-free boundary conditions at the surface and depth boundaries.

For our manufactured solution, we choose $u^*(y, z) = \cos(\frac{\pi y}{L_y})(\cos(\frac{2\pi z}{L_z}) - 1)$. This choice of $u^*(y, z)$ satisfies Eqs. (4.1.1a-4.1.1e) with

$$\begin{aligned}
f(y, z) &= -\mu_1 \cos(\frac{\pi y}{L_y})(\cos(\frac{2\pi z}{L_z}) - 1)(\frac{\pi}{L_y})^2 \dots \\
&\quad + 2\mu_2 \sin(\frac{\pi y}{L_y}) \sin(\frac{2\pi z}{L_z})(\frac{\pi}{L_y})(\frac{2\pi}{L_z}) - \mu_3 \cos(\frac{\pi}{L_y}) \cos(\frac{2\pi}{L_z})(\frac{2\pi}{L_z})^2 \\
g_f &= \cos(\frac{2\pi}{L_z}) - 1 \\
g_r &= 1 - \cos(\frac{2\pi}{L_z}) \\
(\mu_2 \frac{\partial u^*}{\partial y} + \mu_3 \frac{\partial u^*}{\partial z}) \Big|_{z=0} &= (-\mu_1 \frac{2\pi}{L_z} \sin(\frac{2\pi z}{L_z}) \cos(\frac{\pi y}{L_y}) - \mu_2 \frac{\pi}{L_y} \sin(\frac{\pi y}{L_y})(\cos(\frac{2\pi z}{L_z}) - 1)) \Big|_{z=0} = 0 \\
(\mu_2 \frac{\partial u^*}{\partial y} + \mu_3 \frac{\partial u^*}{\partial z}) \Big|_{z=L_z} &= (-\mu_2 \frac{2\pi}{L_z} \sin(\frac{2\pi z}{L_z}) \cos(\frac{\pi y}{L_y}) - \mu_3 \frac{\pi}{L_y} \sin(\frac{\pi y}{L_y})(\cos(\frac{2\pi z}{L_z}) - 1)) \Big|_{z=L_z} = 0
\end{aligned}$$

Eqs. (4.1.1a-4.1.1e) are then discretized as follows

$$\mu_1 \mathbf{D}_{2y} \mathbf{u}^* + 2\mu_2 \mathbf{D}_{zy} \mathbf{u}^* + \mu_3 \mathbf{D}_{2z} \mathbf{u}^* = \mathbf{f} - \mathbf{p}_f - \mathbf{p}_r - \mathbf{p}_s - \mathbf{p}_d \quad (4.1.2)$$

where $\mathbf{f} = f(y_i, z_i)$. In other words, \mathbf{f} is a vector containing the values of $f(y, z)$, restricted to the discrete domain. \mathbf{u}^* is defined in the same manner as \mathbf{u} in the previous section. $\mathbf{D}_{2y}, \mathbf{D}_{zy}, \mathbf{D}_{2z}, \mathbf{p}_f, \mathbf{p}_r, \mathbf{p}_s, \mathbf{p}_d$ are given in the previous section.

The goal is to verify that our discretization of Eqs. (3.0.1-3.0.5) is spatially accurate, by checking that the numerical approximation \tilde{u} converges to u^* , under mesh refinement, with second-order accuracy.

The error, for a given grid spacing h , between the exact solution u^* and the numerical approximation \tilde{u} , in the discrete L_2 -norm is given by

$$\text{Error}(h) = \frac{\|\mathbf{u}^* - \tilde{\mathbf{u}}\|}{\|\mathbf{u}^*\|} \quad (4.1.3)$$

To verify the spatial accuracy of our discretization, we iteratively halve the gridspacing h and compute $\text{Error}(h)$. The rate of convergence is then given by:

$$\log_2 \left(\frac{\text{Error}(h)}{\text{Error}(\frac{h}{2})} \right) \quad (4.1.4)$$

Table 4.1.1 lists the error under successive mesh refinement along with the rate of

convergence. As desired, we achieve second order convergence to the exact solution. Figure 4.1.1 shows a plot of the numerical approximation to the manufactured solution, along with a plot of the exact solution itself.

Table 4.1.1: Error computed in the discrete L_2 norm. The rate of convergence approaches 2 under mesh refinement.

h	N	$\ \tilde{\mathbf{u}} - \mathbf{u}^*\ $	Error(h)	Rate
0.4000	61	0.06119	0.0028961	—
0.2000	121	0.015153	0.00072305	2.0019
0.1000	241	0.003767	0.00018049	2.0022
0.0500	481	0.00093887	4.5077×10^{-5}	2.0014
0.0250	961	0.00023434	1.1263×10^{-5}	2.0008
0.0125	1921	5.8538×10^{-5}	2.8149×10^{-6}	2.0004

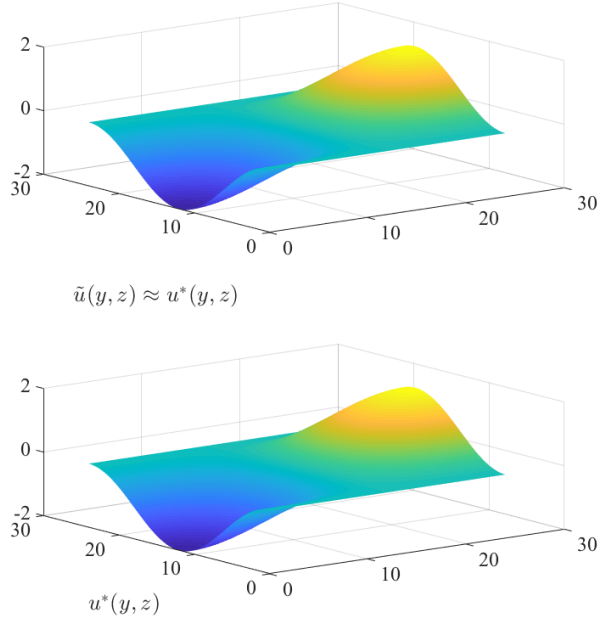


Figure 4.1.1: The numerical solution \tilde{u} is shown along with exact solution u^*

A full treatment of the stability and accuracy in both time and space is given in [5] and [3]. The time stepping method employed in this thesis is the same as the method described in both these papers, as such we elect to omit a treatment of temporal convergence.

5 | Frictional Framework and Time Stepping Method

Now that we've confirmed the spatial accuracy of our method, we turn our attention to evolving the system through time. Modeling the full earthquake cycle over thousands of simulated years is computationally challenging. We motivate our time stepping method with the following example. The Courant-Friedrichs-Lewy (CFL) condition is a necessary condition for convergence when numerically solving certain partial differential equations with finite difference methods.

For an explicit time-marching discretization of the transport equation $\frac{\partial u}{\partial t} + \alpha \frac{\partial u}{\partial x} = 0$ (a prototype for hyperbolic “wave-like” problems) the stability condition is:

$$\left| \frac{\alpha \Delta t}{\Delta x} \right| \leq 1$$

Where α is the propagation velocity of the wave. For seismic waves, propagation velocities tend to range between 2 km/s and 8 km/s.

To illustrate, take $\alpha = 8\text{km/s}$ and grid spacing $\Delta x = 0.1\text{km}$.

$$\begin{aligned} \text{The CFL condition states } & \left| \frac{8\Delta t}{0.1} \right| \leq 1 \\ \text{then } & \Delta t \leq 0.0125 \text{ seconds.} \end{aligned}$$

Which restricts δt to less than 0.0125 seconds in order to maintain stability when time stepping. Taking such small time steps becomes computationally unfeasible when simulating phenomena, such as the earthquake cycle, which happen on time scales of thousands of years.

Instead, we elect to evolve our system with an adaptive time stepping scheme. Rather than solving Eq. 3.0.1, we solve the associated equilibrium equation:

$$0 = \mu_1 \frac{\partial^2 u}{\partial y^2} + 2\mu_2 \frac{\partial^2 u}{\partial y \partial z} + \mu_3 \frac{\partial^2 u}{\partial z^2} \quad (y, z) \in [0, L_y] \times [0, L_z] \quad (5.0.1)$$

Although we neglect inertia when solving Eq. 3.0.1, we approximate inertial effects using radiation damping when accounting for frictional sliding on the fault. This resultant steady state problem is then evolved in time by the time dependant boundary conditions.

At the right boundary $y = L_y$ we enforce a displacement Dirichlet boundary condition to load the system at a rate of V_p , which is on the order of 35 mm/year. Boundary condition

$$g_r = V p_t / 2 \quad (5.0.2)$$

mimics off-fault tectonic loading.

At the left boundary, where our simulated fault is located, we enforce rate-and-state friction, which produces fault slip, imposed via the boundary condition

$$g_f = \Delta u(z, t).$$

(see also [14]).

Let $F(V, \Psi)$ denote fault strength, a function of slip velocity $V(z, t) = \frac{\partial \Delta u}{\partial t}$ and of state variable Ψ . $F(V, \Psi)$ is given by

$$F(V, \Psi) = a \sigma_n \sinh^{-1} \left(\frac{V}{2V_0} e^{\frac{\Psi}{a}} \right). \quad (5.0.3)$$

With radiation damping approximating inertial effects, shear stress at the fault is expressed as

$$\tau = \tau_{qs} - \eta V \quad (5.0.4)$$

where $\tau_{qs} = \left(\mu_1 \frac{\partial u}{\partial y} + \mu_2 \frac{\partial u}{\partial z} \right) \Big|_{y=0}$ and $\eta = \frac{1}{2} \sqrt{\mu_1 \rho}$, is a radiation damping term.

We set shear stress τ equal to fault strength along the fault boundary

$$\tau_{qs} - \eta V = a\sigma_n \sinh^{-1} \left(\frac{V}{2V_0} e^{\frac{\Psi}{a}} \right). \quad (5.0.5)$$

All the pieces are now in place to demonstrate how the system models the fault over a multiple time scales.

The discretization of Eq. 5.0.1 is identical to the right-hand side of Eq. 3.0.1 in Chapter 4

$$\mu_1 \mathbf{D}_{2y} \mathbf{u} + 2\mu_2 \mathbf{D}_{zy} \mathbf{u} + \mu_3 \mathbf{D}_{2z} \mathbf{u} = -\mathbf{p}_f - \mathbf{p}_r - \mathbf{p}_s - \mathbf{p}_d \quad (5.0.6)$$

which yields a linear system of equations, which can be written as $\mathbf{A}\mathbf{u} = \mathbf{b}$.

1. System $\mathbf{A}\mathbf{u} = \mathbf{b}$ is solved with MATLAB's optimized direct solver.
2. Solution \mathbf{u} is used to compute τ_{qs} (5.0.5), the shear stress on the fault. This, in turn, is used to solve $\tau = F(V(t, z), \Psi(t, z))$ for $V(t, z)$ with Newton's method.
3. Slip velocity and state variable Ψ are obtained by numerically integrating the following ODEs with MATLAB's built in 4/5th order Runge-Kutta solver ODE45, using the updated value of $V(t)$.

$$\begin{aligned} \frac{\partial \Delta u}{\partial t} &= V(t, z) \\ \frac{\partial \Psi}{\partial t} &= \frac{bv_0}{D_c} \left[e^{\left(\frac{f_0 - \Psi(t)}{b} \right)} - \frac{V(t)}{V_0} \right] \end{aligned}$$

4. These update values of Ψ , Δu are used in step 1 and 2. The process repeats iteratively.

The rate-and-state frictional framework that we apply to the fault boundary imposes its own conditions on the numerical stability of our problem. Stability of the frictional sliding in our problem requires that the numerical discretization resolve a critical wavelength given by

$$h^* = \frac{2\pi}{k_c r} = \frac{\pi \mu^* D_c}{\sigma_n (b - a)} \quad (5.0.7)$$

where

$$\mu^* = \sqrt{\det \begin{bmatrix} \mu_1 & \mu_2 \\ \mu_2 & \mu_3 \end{bmatrix}} \quad (5.0.8)$$

and

$$k_{cr} = \frac{2(b-a)\sigma_n}{\mu^* D_c}. \quad (5.0.9)$$

Matrix $\begin{bmatrix} \mu_1 & \mu_2 \\ \mu_2 & \mu_3 \end{bmatrix}$ is a matrix of the material stiffness coefficients of the problem, and

k_{cr} is a critical wave number that is related to the critical wave-length h^* . Note that μ^* , h^* , and k_{cr} are straightforward extensions of the analysis in [13].

The aging law for state variable Ψ (see step 2 above) imposes further conditions on numerical stability; a characteristic length scale, $L_b = \frac{\mu^* D_c}{\sigma_n b}$, which must be resolved with sufficient grid points [3].

6 | Simulations

We are now ready to simulate anisotropy in the earthquake cycle. For our simulations we keep intact most of the parameter choices made in [3], for the non basin reference simulations. We choose to increase the the domain size from $L_y = L_z = 24$ km to $L_y = L_z = 72$ km. The domain length of 72 km is 6 times the depth $H = 12$ km, at which the fault begins to transition from velocity-weakening to velocity-strengthening. This choice for domain length is made to ensure that we include at least 90% of the relative motion at the surface [17]. In choosing what values μ_1, μ_2 , and μ_3 ought to take on, we refer to the range of values given in [3], for shear modulus μ . These values are taken from the Southern California Earthquake Center (SCEC) Community Velocity Model of various regions in Southern California, [3], [18]. We choose to keep μ_1, μ_2 , and μ_3 below 36 GPa and above 7 GPa for all of our simulations. Table 6.0.1 shows the parameters used in our simulations.

With the overall range of values for μ_1, μ_2 , and μ_3 chosen, the question becomes, what should μ_1, μ_2 , and μ_3 be, in order to gain a meaningful preliminary understanding of the effect of anisotropy?

We choose to conduct two parameter studies. In the first we model a type of anisotropy called *orthotropic anisotropy*. The orthotropic wave equation is derived by following the steps in Chapter 2 with the orthotropic stiffness tensor, which has only 9 independent entries, substituted in place of the full stiffness tensor. In the 2D anti-plane setting, the resultant equation is equivalent to setting $\mu_2 = 0$ in Eq. 3.0.1. An orthotropic material, is a material that contains two orthogonal planes of symmetry. Within one of these symmetry planes, material subjected to a force deforms identically to all other material in the plane. In other words, restricted to one of these planes of symmetry, the material is isotropic.

In this first parameter study, we hold values of μ_1 constant and decrease μ_3 . Recall that stress component σ_{xz} acts in the z direction, while stress component σ_{xy} acts

in the y direction, and that for 2D anti-plane motion, $\sigma_{xy} = \mu_1 \frac{\partial u}{\partial y} + \mu_2 \frac{\partial u}{\partial z}$, and $\sigma_{xz} = \mu_2 \frac{\partial u}{\partial y} + \mu_3 \frac{\partial u}{\partial z}$. This means that when $\mu_2 = 0$, μ_1 only impacts stress in the z direction, and μ_3 only impacts stress in the y direction. Consequently, as μ_3 decreases the strength of anisotropy relative to the isotropic reference case (i.e. reference case $\mu_1 = \mu_3$, and $\mu_2 = 0$), increases.

For our second parameter study, we set $\mu_1 = \mu_3 = \mu$ and increase μ_2 . In this study, the closer μ_2 is to zero, the closer a simulation is to the isotropic reference, therefore increasing μ_2 increases the relative strength of anisotropy. Since $\mu_2 \neq 0$, σ_{xy} and σ_{xz} do not simplify like they do in the orthotropic case above. In this study $\sigma_{xy} = \mu \frac{\partial u}{\partial y} + \mu_2 \frac{\partial u}{\partial z}$, and $\sigma_{xz} = \mu_2 \frac{\partial u}{\partial y} + \mu \frac{\partial u}{\partial z}$. Because μ and μ_2 appear in both of the components of stress, σ_{xz} and σ_{xy} , these influence the stress in each of the y and z directions. It is important to note that μ and μ_2 act on different terms in each of the stress components, so the stresses are not equal in the z and y directions.

Table 6.0.1: Parameters used in Earthquake cycle simulations

Parameter	Value
L_y	72 km
L_z	72 km
H	12 km
μ_1	variable (GPa)
μ_2	variable (GPa)
μ_3	variable (GPa)
ρ	2800 kg/m ³
σ_n	50 MPa
a	0.015
b	depth variable
D_c	8 mm
V_p	10 ⁻⁹ m/s
V_0	10 ⁻⁶ m/s
f_0	0.6
τ^∞	24.82 MPa

6.1 Parameter Study 1

The results of parameter study 1 are presented in Fig. 6.1.1 and Fig. 6.1.2, which show profiles of cumulative slip as μ_3 is decreased, as well the maximum slip velocities of the simulations over time, shown together in one figure for comparison purposes. In the cumulative slip profiles, slip is plotted in blue during the interseismic period, when the maximum velocity ≤ 1 mm/s, and every second in red during a quasi-dynamic event, when the maximum velocity ≥ 1 mm/s. Maximum velocity is taken over the whole fault. As μ_3 decreases relative to the isotropic reference the amount of accumulated slip increases and the recurrence interval increases.

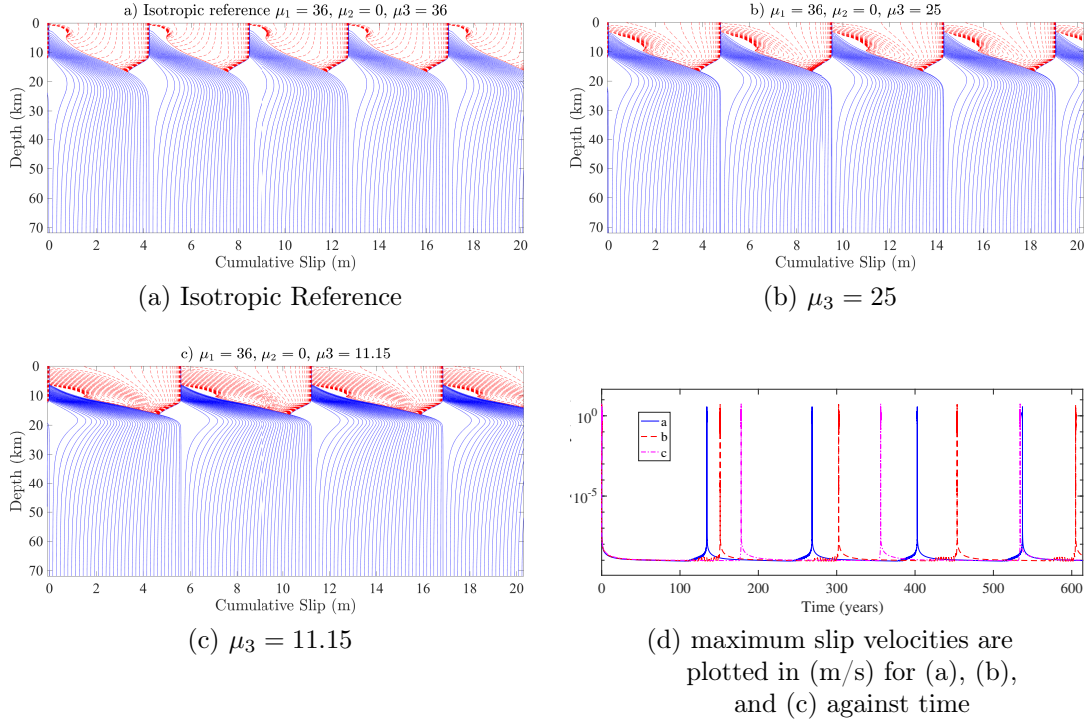


Figure 6.1.1: (a) through (c) show snapshots of cumulative slip profiles as μ_3 is decreased. Slip during the interseismic period, when maximum velocity ≤ 1 mm/s, is plotted in blue in 5 year intervals. Slip during a simulated earthquake rupture is plotted in red in 1 second intervals.

Comparing Fig. 6.1.1(a) and Fig. 6.1.1(b) we see that decreasing μ_3 from 36 GPa to 25 GPa, increases slip and recurrence interval only slightly. Fig. 6.1.1(a) accumulates around 4 meters of slip during each event, while Fig. 6.1.1(b) accumulates a little over 4 meters of slip per event. Their respective interseismic periods are around 125,

and 150 years. Comparing Fig. 6.1.1(a) to Fig. 6.1.1(c) we see that dropping μ_3 from 36 to 11.15 increases slip and recurrence interval more dramatically. Events in Fig. 6.1.1(c) accumulate a little under 6 meters of slip per event, and the recurrence interval increases to just under 200 years.

To control for the influence on recurrence interval of characteristic wave-length h^* (see 5.0.7) we reduce μ_1 to 32, and compare this new isotropic reference to a simulation where $\mu_1 = 32$, and $\mu_3 = 7.1$.

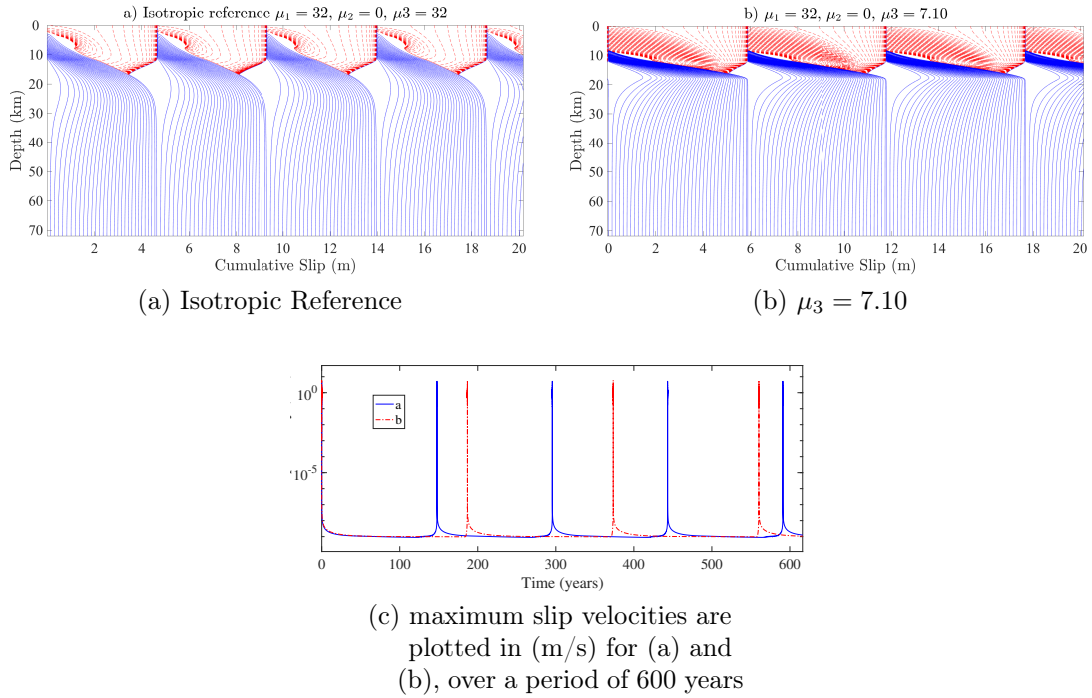


Figure 6.1.2: Cumulative slip plotted against depth for (a) the isotropic case and (b) μ_3 decreased to 7.10. Slip during the interseismic period, when maximum velocity ≤ 1 mm/s, is plotted in blue in 5 year intervals. Slip during a simulated earthquake rupture is plotted in red in 1 second intervals.

Decreasing μ_1 to 32 changes the value of μ^* (see 5.0.8) which h^* depends on. Compare Fig. 6.1.1(c) to Fig. 6.1.2(b), the parameters in Fig. 6.1.2(b) yield a $\mu^* \approx 15$, while those in Fig. 6.1.1(c) yield a $\mu^* \approx 20$. If the recurrence interval was influenced by μ^* alone, we'd expect to see a longer recurrence interval for Fig. 6.1.2(b) than for Fig. 6.1.1(c), however they both have a recurrence interval of just under 200 years.

6.2 Parameter Study 2

Our results for parameter study 2 are presented in Fig. 6.2.1, Fig. 6.2.2, and Fig. 6.2.3. In Fig. 6.2.1 we keep $\mu_1 = \mu_3 = 32$ and increase μ_2 . As with the orthotropic case, increasing the anisotropy relative to the isotropic reference increases the recurrence interval, and the cumulative slip per event. Fig. 6.2.1(b) shows that cumulative slip has increased from just under 5 meters per event in the isotropic reference case, to around 7 meters per event when μ_2 is increased to 11.14. In Fig. 6.2.1(c) we see that increasing μ_2 to 18 has caused the simulated fault to exhibit period doubling, where events of alternating size occur every other rupture.

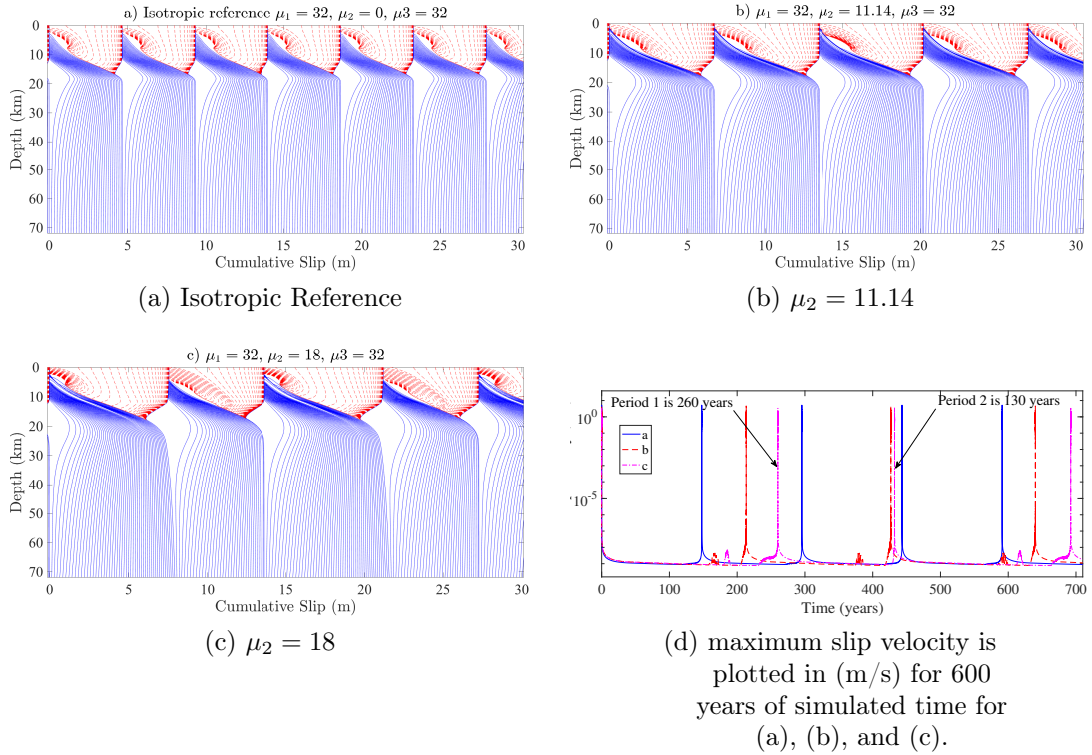


Figure 6.2.1: (a) through (c) show snapshots of cumulative slip profiles as μ_2 is increased. Slip during the interseismic period, when maximum velocity ≤ 1 mm/s, is plotted in blue in 5 year intervals. Slip during a simulated earthquake rupture is plotted in red in 1 second intervals. In (d) observe that spikes in maximum slip velocity (i.e. earthquake events) for simulation (c) recur on an alternating schedule, every 260 and every 130 years.

Events with period 1 (see Fig. 6.2.1) accumulate 7 or 8 meters of slip, while events of period 2 about 5 meters of slip. Period 1 events occur 260 years after a Period

2 event, whereas Period 2 events occur 130 after a Period 1 event. Period 1 events nucleate much closer to the surface, at a depth between 2 and 8 km, compared to a nucleation zone of between 5 and 10 km depth for Period 2 events. This suggests that after a Period 2 event, slip near the surface over a smaller, shallower area is able to nucleate an event, but that after a Period 1 event, a deeper, larger section of the fault must slip to nucleate quasi-dynamic rupture.

At the present time it is difficult to say what about the parameter choice in Fig. 6.2.1(c) led to the observed period doubling. In an effort to examine whether the period doubling was the result of the ratio of μ_1 to μ_2 , we decreased μ_2 to 16, and found that choosing $\mu_1 = 28.\bar{4}$ preserved the ratio of μ_1 to μ_2 found in Fig. 6.2.1(c). This simulation further supports our preliminary observations that increasing anisotropy relative to an isotropic reference increases both slip per event and the recurrence interval, however, it does not exhibit period doubling. This suggests that the ratio of μ_1 to μ_2 is not by itself enough to cause period doubling. Further investigation is warranted, but is outside the scope of this thesis. Fig. 6.2.2 shows the results for $\mu_1 = 28.\bar{4}$ and $\mu_2 = 16$ next to the appropriate isotropic reference.

Fig. 6.2.3 presents simulations where μ_2 is increased relative to a static $\mu_1 = \mu_3 = 36$. No period doubling occurs, but once again, as μ_2 increases so does amount of slip per event and length of the recurrence interval between events. In Fig. 6.2.3(b) we see events nucleating at the surface, it is possible that this is a numerical artifact, as in this simulation h^* and L_b were resolved with fewer grid-points than in other simulations.

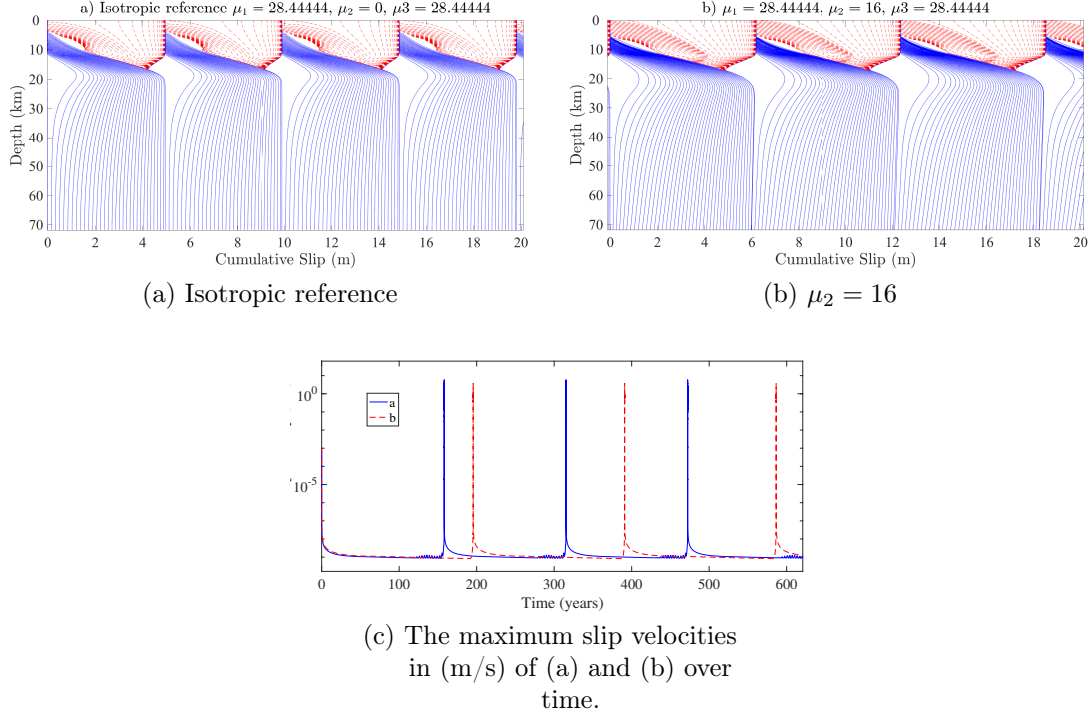


Figure 6.2.2: (a) shows a snapshot of the cumulative slip profile for the isotropic reference case. (b) shows a snapshot of the cumulative slip profile when μ_2 is increased to 16. The ratio of μ_1 to μ_2 in (b) is identical to the ratio of μ_1 to μ_2 in Figure 6.2.1(c)

6.3 Conclusion

We have developed and implemented a method for studying anisotropy in the earthquake cycle. The initial results presented in this thesis suggest that increasing the degree of anisotropy extends the recurrence interval, relative to the isotropic reference, leading to larger amounts of slip per rupture. Additionally, our initial observations suggest that anisotropy may in certain instances lead to period doubling. This initial study successfully demonstrates the need for further investigation, and suggests directions for further study. The scope of this initial study is insufficient to explain the observed period doubling and nucleation near the surface that occurs with particular parameter choices. Further work should refine on parameter studies 1 and 2 in order to reproduce and explain the observations presented here. Additionally, while informative as a starting point, assuming homogenous constant anisotropic material properties is not very realistic. Further work is needed to investigate non-constant choices for μ_1 , μ_2 , and μ_3 . In future work, we plan to develop the method to cre-

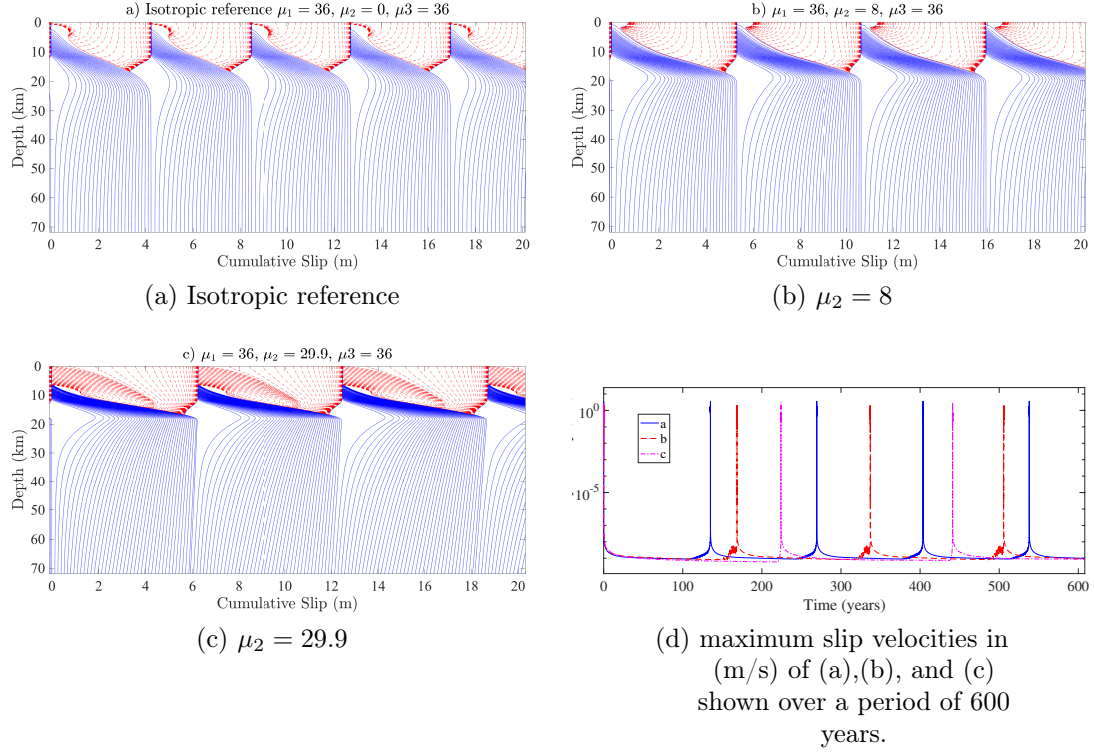


Figure 6.2.3: Snapshots of the cumulative slip profiles for $\mu_1 = \mu_3 = 36$. μ_2 is increased relative to (a), in (b) and (c). (d) provides a comparison of event recurrence by showing the maximum slip velocities of (a)-(c) on one plot.

ate anisotropic layers in the material around a fault, particularly in layering strong anisotropy close to the fault with a transition to isotropy off-fault. We are interested in learning whether anisotropy can be used to explain observed surface deformation, or perhaps reconcile discrepancies in estimates of fault locking depth. We present this thesis as a proof of concept, and an initial step towards this goal.

Bibliography

- [1] Crampin, S., Gao, Y., and Bukits, J. (2015). A review of retrospective stress-forecasts of earthquakes and eruptions. *Physics of the Earth and Planetary Interiors*, 245:76 – 87.
- [2] Crampin, S. and Lovell, J. H. (1991). A decade of shear-wave splitting in the earth’s crust: what does it mean? what use can we make of it? and what should we do next? *Geophysical Journal International*, 107(3):387–407.
- [3] Erickson, B. A. and Dunham, E. M. (2014). An efficient numerical method for earthquake cycles in heterogeneous media: Alternating subbasin and surface-rupturing events on faults crossing a sedimentary basin. *Journal of Geophysical Research: Solid Earth*, 119(4):3290–3316.
- [4] Erickson, B. A., Dunham, E. M., and Khosravifar, A. (2017). A finite difference method for off-fault plasticity throughout the earthquake cycle. *Journal of the Mechanics and Physics of Solids*, pages see–<https://doi.org/10.1016/j.jmps.2017.08.002>.
- [5] Erickson, B. A. and Nordström, J. (2014). Stable, high order accurate adaptive schemes for long time, highly intermittent geophysics problems. *Journal of Computational and Applied Mathematics*, 271:328 – 338.
- [6] Fernández, D. C. D. R., Hicken, J. E., and Zingg, D. W. (2014). Review of summation-by-parts operators with simultaneous approximation terms for the numerical solution of partial differential equations. *Computers Fluids*, 95:171 – 196.
- [7] Gustafsson, B., Kreiss, H.-O., and Olinger, J. (2013). *Time-dependent problems and difference methods; 2nd ed.* Pure and applied mathematics a wiley series of texts, monographs and tracts. Wiley, Somerset.

- [8] Hicken, J. E. and Zingg, D. W. (2013). Summation-by-parts operators and high-order quadrature. *Journal of Computational and Applied Mathematics*, 237(1):111–125.
- [9] Kaselow, A. (2004). *The Stress Sensitivity Approach: Theory and Application: Der Spannungs-Sensitivitäts-Ansatz: Theorie und Anwendung*.
- [10] Long, M. D. and Becker, T. W. (2010). Mantle dynamics and seismic anisotropy. *Earth and Planetary Science Letters*, 297(3):341 – 354.
- [11] Mattsson, K. (2012). Summation by parts operators for finite difference approximations of second-derivatives with variable coefficients. *Journal of Scientific Computing*, 51(3):650–682.
- [12] Ranjith, K. (2008). Dynamic anti-plane sliding of dissimilar anisotropic linear elastic solids. *International Journal of Solids and Structures*, 45(14):4211–4221.
- [13] Ranjith, K. and Gao, H. (2007). Stability of frictional slipping at an anisotropic/isotropic interface. *International journal of solids and structures*, 44(13):4318–4328.
- [14] Rice, J. R., Lapusta, N., and Ranjith, K. (2001). Rate and state dependent friction and the stability of sliding between elastically deformable solids. *Journal of the Mechanics and Physics of Solids*, 49(9):1865–1898.
- [15] Roache, P. J. (1998). *Verification and validation in computational science and engineering*, volume 895. Hermosa Albuquerque, NM.
- [16] Savage, J. and Burford, R. (1973a). Geodetic determination of relative plate motion in central california. *Journal of Geophysical Research*, 78(5):832–845.
- [17] Savage, J. C. and Burford, R. O. (1973b). Geodetic determination of relative plate motion in central california. *Journal of Geophysical Research*, 78(5):832–845.
- [18] Tape, C., Liu, Q., Maggi, A., and Tromp, J. (2009). Adjoint tomography of the southern california crust. *Science*, 325(5943):988–992.
- [19] Virta, K. and Mattsson, K. (2014). Acoustic wave propagation in complicated geometries and heterogeneous media. *Journal of Scientific Computing*, 61(1):90–118.